Frontiers of Information Technology & Electronic Engineering
www.jzus.zju.edu.cn; engineering.cae.cn; www.springerlink.com
ISSN 2095-9184 (print); ISSN 2095-9230 (online)
E-mail: jzus@zju.edu.cn

Deep learning based wavefront sensor for complex wavefront detection in adaptive optical microscopes[*]

Shuwen HU[§1,2], Lejia HU[§1,2], Wei GONG[†‡3], Zhenghan LI[1,2], Ke SI[†‡1,2,3]

[1]*Department of Neurology of the First Affiliated Hospital, State Key Laboratory of Modern Optical Instrumentation,*
Zhejiang University School of Medicine, Hangzhou 310009, China
[2]*College of Optical Science and Engineering, Zhejiang University, Hangzhou 310027, China*
[3]*Research Units for Emotion and Emotion Disorders, Chinese Academy of Medical Sciences,*
MOE Frontier Science Center for Brain Research and Brain-Machine Integration,
School of Brain Science and Brain Medicine, Zhejiang University, Hangzhou 310058, China
[†]E-mail: weigong@zju.edu.cn; kesi@zju.edu.cn

Received Aug. 21, 2020; Revision accepted Dec. 17, 2020; Crosschecked Jan. 25, 2021; Published online Mar. 29, 2021

Abstract: The Shack-Hartmann wavefront sensor (SHWS) is an essential tool for wavefront sensing in adaptive optical microscopes. However, the distorted spots induced by the complex wavefront challenge its detection performance. Here, we propose a deep learning based wavefront detection method which combines point spread function image based Zernike coefficient estimation and wavefront stitching. Rather than using the centroid displacements of each micro-lens, this method first estimates the Zernike coefficients of local wavefront distribution over each micro-lens and then stitches the local wavefronts for reconstruction. The proposed method can offer low root mean square wavefront errors and high accuracy for complex wavefront detection, and has potential to be applied in adaptive optical microscopes.

Key words: Adaptive optics; Wavefront detection; Deep learning; Zernike coefficients; Microscopy
https://doi.org/10.1631/FITEE.2000422 **CLC number:** O439

1 Introduction

Fluorescence microscopes enable the observation of specimen structure and function in biomedical research (Cornea and Conn, 2014). Over the past few decades, several super resolution optical microscopes have been developed to overcome the imaging resolution limitation (Zeng et al., 2017; Wang BK et al., 2019). To better investigate and analyze the biological phenomena, deep imaging penetration becomes significant. However, the spatially varying refractive index in biological specimens limits the penetration depth and imaging quality of optical microscopes.

As an effective way to detect and compensate for optical aberration, adaptive optics (AO) has been applied to improve the imaging performance of fluorescence microscopes (Ji, 2017). The main idea of AO is to measure the wavefront aberrations precisely and then compensate for them accordingly. There are two commonly used strategies, direct and indirect wavefront sensing, to implement AO in fluorescence microscopes. The former detects the aberrations through a wavefront sensor, such as the Shack-Hartmann wavefront sensor (SHWS) (Rodríguez and Ji, 2018). The latter offers a sensorless strategy, such

---

[‡] Corresponding authors

[§] These authors contributed equally to this work

[*] Project supported by the National Natural Science Foundation of China (Nos. 61735016, 81771877, and 61975178), the Zhejiang Provincial Natural Science Foundation of China (No. LR20F050002), the Key R&D Program of Zhejiang Province, China (No. 2021C03001), the CAMS Innovation Fund for Medical Sciences, China (No. 2019-I2M-5-057), and the Fundamental Research Funds for the Central Universities, China

ORCID: Wei GONG, https://orcid.org/0000-0003-3969-5607; Ke SI, https://orcid.org/0000-0001-8328-4325

as image-based wavefront sensing (Booth, 2014). However, these two strategies have limitations. The SHWS-based strategy has the capability of fast wavefront detection, which is suitable for real-time biological imaging but only in transparent or weakly scattering samples (Wang K et al., 2014). For deep imaging penetration, the heterogeneous biological specimens could lead to complex speckle patterns on the SHWS, and these yield inaccurate wavefront slope measurements and thus incomplete compensation (Wang K et al., 2014). The indirect wavefront sensing strategy has been successfully applied in biological imaging (Booth et al., 2002; Park et al., 2017), optical focusing (Cui, 2011; Hu LJ et al., 2020), image processing (Li et al., 2020), and optogenetics (Yoon et al., 2015), but the time it takes to reach the optimal corrective wavefront cannot be neglected. Using a segmented deformable mirror (DM) can improve the wavefront detection speed, but increase the cost of the system (Tang et al., 2012).

In recent years, the convolutional neural network (CNN) has been adopted in wavefront sensing. Several studies use CNN to analyze the distorted point spread function (PSF) of the optical system to estimate the corresponding Zernike mode coefficients or to predict the wavefront distribution (Jin et al., 2018; Paine and Fienup, 2018; Cheng et al., 2019; Nishizaki et al., 2019; Vanberg et al., 2019; Cumming and Gu, 2020). However, these methods still require one or more cameras as the detectors, and it is difficult to obtain PSFs in some biological applications, such as in vivo deep tissue imaging. As for SHWS, by scanning the guide star inside a small region, the measured average wavefront can offer effective compensation (Wang K et al., 2014, 2015; Liu TL et al., 2018; Liu R et al., 2019).

Recently, CNN has been applied in SHWS to improve wavefront sensing performance. Gómez et al. (2018) applied a CNN to predict the centroids for wavefront reconstruction from an SHWS pattern. Swanson et al. (2018) used x and y wavefront slopes from SHWS to reconstruct the wavefront with a modified U-net. Dubose et al. (2020) proposed a CNN named ISNet to reconstruct the wavefront with wavefront slopes and the intensity summations from each sub-aperture in SHWS. However, these studies still use centroid positioning or wavefront slope measurements to reconstruct the wavefront. For biological imaging, the guide star in deep tissue would lead to complex speckle patterns on SHWS. This makes it challenging to measure the wavefront slopes. In our previous work, CNNs were used to predict Zernike mode coefficients from an SHWS pattern directly, and the wavefront detection performance when focusing through the mouse brain slice was demonstrated (Hu LJ et al., 2019; Hu SW et al., 2020).

However, some aberrations induced by the thick tissue have complex distributions, which cannot be characterized by limited Zernike polynomial modes. As an alternative, the combination of local wavefront detection and wavefront stitching can reduce the difficulty of complex wavefront detection using an SHWS.

Here, we propose a deep learning based wavefront detection method, two-step wavefront detection (TSWD), to reconstruct the complex wavefront from an SHWS pattern. The main idea of our strategy is to combine the PSF image based Zernike coefficient prediction with wavefront stitching. A CNN is designed to estimate the first 28 coefficients of Zernike square polynomials to reconstruct the local wavefront over each sub-aperture, and another CNN is implemented for global wavefront retrieval. In this way, SHWS can be used to detect wavefront with complex distribution. The proposed method is compatible with a commonly used SHWS, and does not require any change to the system. The wavefront detection performances of this method, such as the root mean square (RMS) wavefront error, peak-to-valley (PV) value, peak-to-background ratio (PBR), and detection speed, are evaluated by comparison with those of conventional wavefront reconstruction methods and an indirect wavefront sensing method. Wavefronts beyond the training range are used to examine the generalization ability of this method.

2 Methods

2.1 Data generation and wavefront detection processes

The commonly used conventional wavefront reconstruction methods for SHWS are modal and zonal approaches, which require wavefront slope measurements from the spot array (Dai, 2008). Previous work has demonstrated that CNNs can predict the Zernike mode coefficients from the SHWS pattern (Hu LJ et al., 2019; Hu SW et al., 2020). However, when using SHWS for complex wavefront detection, such as biological samples, the spot patterns become distorted or even have no effective centroids for positioning, and this limits the application of SHWS. To improve the detection capability of SHWS, we generated a series of complex wavefronts for network training and evaluation. In practical applications, a point light source, such as a fluorophore, serves as a guide star behind the sample, and the aberration induced by the sample is conjugated to the rear pupil of the objective lens for further detection. Here, we used the multiplication of a two-dimensional Gaussian function and the Fourier spectrum of a random matrix to simulate the aberration over the objective lens (Schott et al., 2015).

The wavelength of the guide star was set to 532 nm, which is close to the emission wavelength of the widely used fluorophores. The wavefront range was set to [−2π, 2π] (with a PV value of 2λ, where λ=532 nm), and the complexity of the wavefront distribution could be changed by adjusting the width of the Gaussian function. The generated wavefront was conjugated to the pupil plane of the micro-lens array (MLA) for SHWS pattern generation or wavefront detection (Fig. 1). In this work, 12×12 micro-lenses (about 124 effective regions) were used in the SHWS (384×384 pixels). The corresponding SHWS patterns were generated by numerical simulations with MATLAB. To improve the robustness and generalization of TSWD, Gaussian noise (variance of 10^{-5}) and Poisson noise were added after normalizing the SHWS patterns. Then each sub-region of the SHWS patterns and their corresponding wavefronts were segmented according to the coordinates of the ideal SHWS spot array. Sub-regions with illumination coverage less than 10% were ignored during training and detection. The segmented local wavefronts were one-to-one decomposed with the first 28 Zernike square polynomials, which can be expressed as (Mahajan and Dai, 2007)

$$\psi_{\text{phase}}(x, y)=c_1S_1(x, y)+c_2S_2(x, y)+\ldots+c_{28}S_{28}(x, y)+\ldots,$$

where $\psi_{\text{phase}}(x, y)$ is the square wavefront from the sub-aperture, $S_n(x, y)$ the n^{th} square Zernike mode, and c_n the n^{th} square Zernike mode coefficient. The coefficient of the Piston term was set to zero because it does not affect the local wavefront distribution. For those sub-regions with incomplete illumination coverage, the missing wavefront value was filled with the average value inside the corresponding sub-aperture. Each sub-region of the SHWS patterns and their corresponding square Zernike mode coefficients were used for Net1 training. Then the trained Net1 could be used to estimate the coefficients of sub-regions from a series of new SHWS patterns. The square wavefronts for each sub-aperture were formed by the predicted coefficients and then stitched according to the original coordinates. Although the local wavefront for each sub-aperture could be detected by Net1, their local Piston terms still require compensation. In this case, Net2 was trained with the stitched wavefronts and the original ones for wavefront retrieval. The main process of wavefront detection is given in Fig. 1.

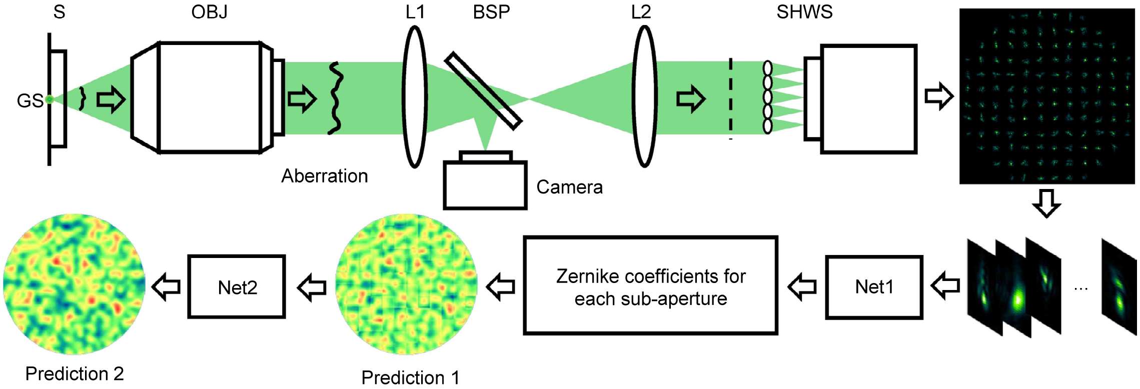

Fig. 1 Illustration of the two-step wavefront detection

S: sample; GS: guide star; L1 and L2: lenses; BSP: beam splitter plate; OBJ: objective lens. The dotted line indicates the pupil plane of the micro-lens array. Prediction 1 indicates the preliminary detected wavefront, and prediction 2 indicates the final wavefront with continuous distribution

Here, 2478 datasets (with 307 200 sub-regions) were generated for Net1 training and 32 760 datasets for Net2 training. Ten percent of the datasets were used for validation. The network training was performed under Keras with TensorFlow backend (Python 3.6.9) on a desktop workstation (Intel Core i9-7920X CPU, NVIDIA RTX 2080 Ti).

2.2 Architectures of convolutional neural networks

To use the intensity distributions of the SHWS spots for wavefront detection and reconstruction, we designed a CNN (Net1) to estimate the first 28 coefficients of Zernike square polynomials. The number of Zernike modes used here was determined through wavefront decomposition and statistical analysis. The architecture of Net1 is illustrated in Fig. 2a. Unlike the CNN used in our previous work, the corresponding sub-region of each sub-aperture had a small image size (32×32). Here, the first two levels of Net1 were used for up-sampling, each level consisting of an up-sampling layer with a 2×2 kernel size (with a stride of 2) to adjust the size and channels of the inputs, followed by a convolutional layer with a 3×3 kernel size, batch normalization (BN), and a rectified linear unit (ReLU). To ensure the robustness and accuracy of the network, the next five convolutional stages and three fully-connected layers were designed for feature extraction and regression. In detail, some stages contained two branches with different kernel sizes (3×3 and 5×5) to make multi-scale feature fusion (concatenate), which enlarges the receptive field of the network. BN and ReLU were followed by every convolutional layer to accelerate convergence. The results from the former stages were flattened and sent to the three fully-connected layers, which were separately activated by ReLU, ReLU, and a linear function. Finally, the fully-connected layers outputted 27 parameters, which correspond to the predicted coefficients of Zernike square polynomials. During the

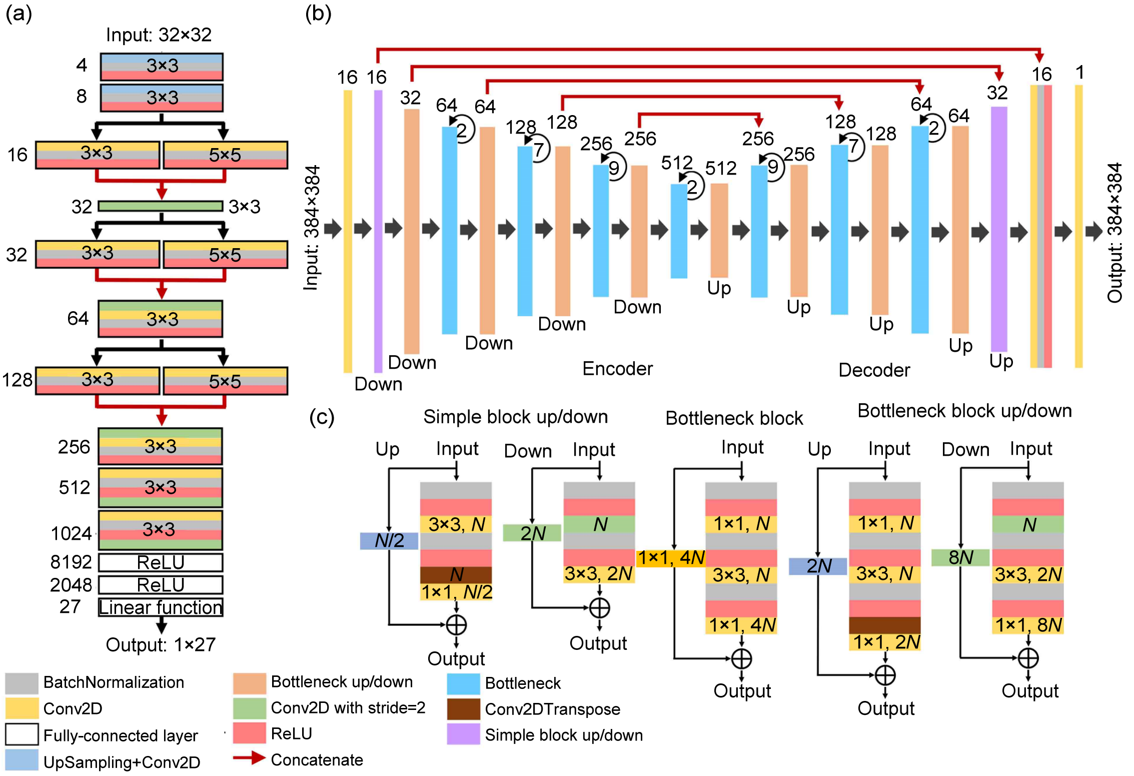

Fig. 2 Illustration of convolutional neural network architectures

(a) Architecture of Net1 (Numbers on the left side indicate the channel numbers for each level; convolutional kernel sizes are given in the corresponding levels); (b) Architecture of Net2 (Numbers over each level indicate the channel numbers set to the corresponding blocks; numbers inside the circular arrows indicate the numbers of repeated operations; "down" and "up" indicate the down-sampling and up-sampling operations, respectively); (c) Details of the blocks used in Net2 (Channel numbers and kernel sizes are given in the corresponding layers). References to color refer to the online version of this figure

Net1 training, Adam was used as the optimizer with an initial learning rate of 10^{-4}, and the learning rate decayed with iterations. The log–cosh function was used as the loss function to increase the robustness of Net1.

The predicted Zernike coefficients from Net1 were used to reconstruct the local wavefronts for every sub-aperture, and then the preliminary predicted wavefront was obtained. However, Piston errors exist between sub-apertures. Therefore, we proposed another CNN (Net2) to retrieve the final continuous wavefront at the pixel level from the preliminary predicted one. The architecture of Net2 was derived from previous work, which combines ResNet with a fully convolutional network (Drozdzal et al., 2016), as shown in Fig. 2b. Net2 contains five kinds of residual blocks, as illustrated in Fig. 2c. All the blocks apply pre-activation (BN followed by ReLU and a convolutional layer) for the input feature maps. The number of initial channels for each block is given, and each bottleneck block has a certain repetition number. The blocks in the decoder path were concatenated with feature maps outputted by the corresponding levels in the encoder path, to speed up the convergence of the network. Different from the original architecture, the weights of each convolutional layer were initiated by “he_normal” and the initial channel numbers of each block were adjusted to better retrieve the wavefront distribution. Each max-pooling layer was replaced by a convolutional layer with a 3×3 kernel size (with a stride of 2) to reduce the loss of information during propagation. The SoftMax classifier was removed to produce a continuous wavefront regression. During the Net2 training, Adam was used as the optimizer with an initial learning rate of 5×10^{-5} and the learning rate decayed with iterations. The RMS wavefront error between the prediction and ground truth was used as the loss function to strongly penalize the slight difference.

3 Results

The proposed TSWD aims to detect the wavefront with a complex distribution. It first performs local wavefront reconstruction for each sub-aperture over SHWS and then stitches the partition wavefronts to reconstruct the overall distribution. In this way, the intensity distributions of the distorted spots or speckle patterns on the SHWS are efficiently used. This can provide more accurate sensing than the centroid positioning and slope measurements. To demonstrate the wavefront detection capability of TSWD and compare it with those of existing methods, we generated another 50 datasets (wavefronts and their corresponding SHWS patterns) for evaluation. These are different from the training datasets.

A set of comparison results in wavefront detection and compensation is given in Fig. 3. As shown in Fig. 3a, most SHWS spots are so strongly distorted that it is difficult to position the centroids and calculate the local wavefront slopes. Since Zernike coefficients are insufficient to characterize the complex wavefront, these kinds of SHWS patterns limit the methods that rely on Zernike coefficient detection, and it becomes difficult to predict the accurate Zernike coefficients through our previous work (Hu LJ et al., 2019; Hu SW et al., 2020). ISNet is a recently proposed method that uses both wavefront slopes and the intensity summation of each sub-aperture to reconstruct the wavefront through deep learning (Dubose et al., 2020). Here, to compare the wavefront detection performances of TSWD and a recently proposed learning based method, we reproduced ISNet which does not rely on Zernike coefficients but predicts wavefront directly. The same training datasets as in TSWD were used to train ISNet. To obtain the inputs of ISNet, we extracted x and y slopes in every sub-region by morphological image processing and centroid positioning. Intensity in sub-regions was calculated by integration. To visually present the detection results of TSWD, we presented the residuals of the detected wavefronts from Net1 and Net2. It is clear that after compensation with the wavefront reconstructed by Net1, the residual in each sub-aperture becomes flat and the intensity distribution of the PSF is concentrated toward the center, but the Piston errors among these sub-apertures cannot be ignored. After wavefront retrieval with Net2, the complex wavefront can be efficiently compensated for and a bright focusing spot can be obtained. As for the conventional methods, the wavefronts reconstructed by the modal (with the first 66 Zernike modes) and zonal approaches are very different from the original one because of the missing details, as shown in Fig. 3b.

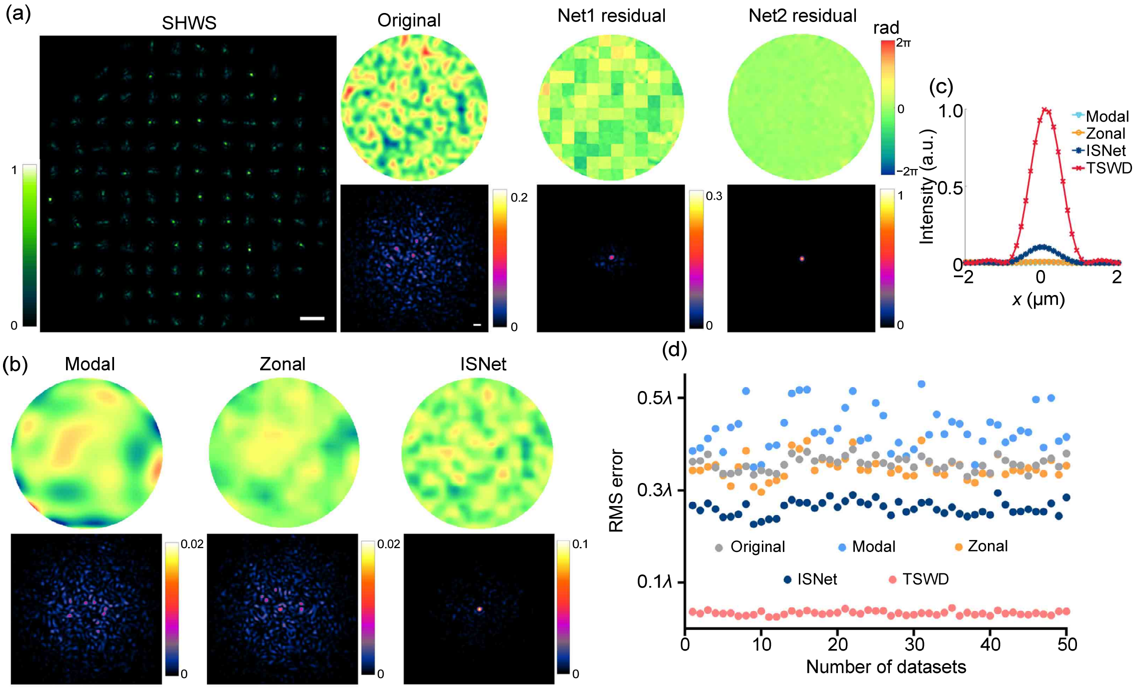

Fig. 3 Comparison results of wavefront detection

(a) Compensation results of Net1 and Net2 (The SHWS pattern is given on the left side with a scale bar of 500 μm; the original wavefront and the wavefront residual after compensation with the predicted wavefront from Net1 and Net2 are given; below the wavefronts are their corresponding focusing results with a scale bar of 3 μm); (b) Detection results of conventional methods and ISNet (Below the wavefronts are the focusing results after compensation with the corresponding methods); (c) Central intensity profiles of different methods; (d) Statistical results of the RMS wavefront errors of different methods. References to color refer to the online version of this figure

After compensation using ISNet, the intensity distribution of the PSF tends to the center, but the peak intensity is much lower than that of TSWD. The focusing results of the other three methods present insufficient detection of the complex wavefront, and the central intensity profiles in Fig. 3c give an intuitive comparison of peak intensity after compensation. Fig. 3d displays the statistical results of the RMS wavefront errors of these methods. The RMS wavefront error of TSWD (0.0338λ) is 92.17% lower than that of the modal approach (0.4314λ), 90.30% lower than that of the zonal approach (0.3483λ), and 87.05% lower than that of ISNet (0.2611λ). This means that TSWD is suitable for detecting the wavefront with a complex distribution. The detection speed is important for the wavefront reconstruction method. Here, the averaged time taken by TSWD to detect a complex wavefront (384×384) from an input SHWS pattern is 0.1385 s, which is about 1.42% faster than the modal approach (0.1405 s). However, because of the different detection mechanisms, the zonal approach (0.1181 ms) and ISNet (38.57 ms) have faster detection speed. Considering that these two approaches are far less accurate than TSWD, this gap in detection speed is acceptable.

To further evaluate the wavefront detection capability of TSWD, we generated a series of wavefront groups with different PV values. PV values of these wavefronts vary from 1λ to 3λ, each group containing nine datasets. Fig. 4 presents two sets of comparison with four methods. The first set of comparisons shown in Fig. 4a has a PV value of 1λ, and the spots on the SHWS are still tight enough for centroid positioning. However, the conventional methods and ISNet failed to detect the complex distribution of the local wavefronts, resulting in an incomplete compensation. As a comparison, the predicted wavefront of TSWD could well compensate for the original one. From this comparison, we can see that the complex wavefront with a small PV value would not seriously distort the PSF, but the focal intensity of the PSF would clearly decrease, which reveals the importance

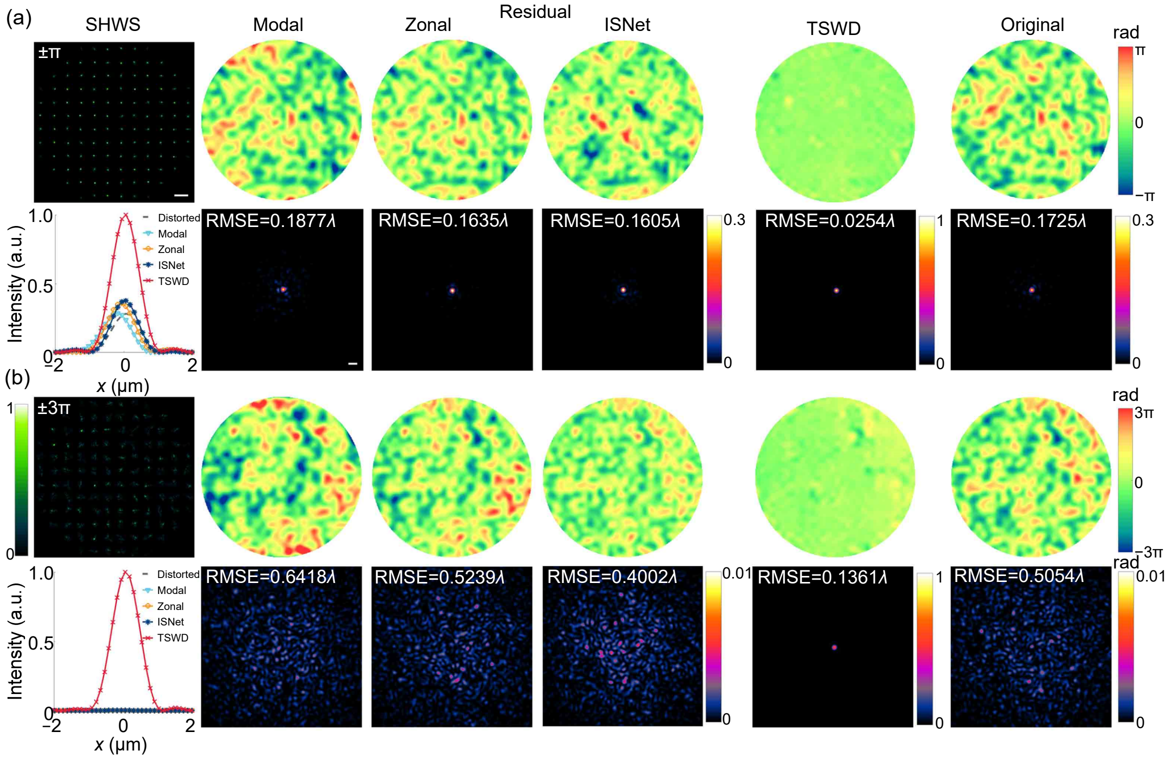

Fig. 4 Comparison results of wavefront detection with different PV values

(a) Compensation results with a PV value of 1λ (The SHWS pattern is given on the left side with a scale bar of 500 μm; the wavefront residual after compensation and the original wavefront are given accordingly; below the wavefronts are the corresponding focusing results with a scale bar of 3 μm; the central intensity profiles of the compensated foci are given on the left side); (b) Compensation results with a PV value of 3λ. References to color refer to the online version of this figure

of wavefront distribution detection on every sub-aperture. Another set of comparisons with a PV value of 3λ is given in Fig. 4b. In this comparison, the PV value is beyond the training range of our networks, and most spots on the SHWS become speckle patterns. However, our method could offer an acceptable compensation result, while the conventional methods and ISNet failed to detect the wavefront. Furthermore, in these comparisons, the wavefront residuals of the modal approach are significantly larger than those of the zonal approach. This means that the modal approach is more sensitive to the complex wavefronts. Since the modal approach has been widely adopted in adaptive optical microscopes, this limitation would degrade its performance in deep tissue imaging.

To better compare the performances of these methods, we calculated the RMS wavefront errors and the residual wavefront PV values of four methods with different input wavefront PV values. The trends of the compensation results are given in Fig. 5. From the line charts, we found that the wavefront residuals of four methods increase as the input wavefront PV value increases, but the residuals of TSWD are much lower than those of other methods. When detecting the complex wavefronts beyond the training range, TSWD could offer an acceptable result, while the other mentioned methods performed poorly. The intensity distortions of spots in SHWS are related to PV values. Since the complex wavefront decreases the completeness of the SHWS pattern, the accuracy of centroid positioning and the performance of deep learning based wavefront sensing are both degraded.

It is seen that direct wavefront sensing failed in complex wavefront detection and reconstruction. However, indirect wavefront sensing always has a better performance in overcoming severe optical scattering. Examples of such sensing are the coherent optical adaptive technique (COAT) and digital optical phase conjugation (DOPC) (Cui, 2011; Yu et al., 2019; Hu LJ et al., 2020). Therefore, we compared TSWD with COAT which has been applied in optical focusing. We divided the incident wavefront into 12×12 (132 effective), 24×24 (484 effective), and 32×32 (856 effective) segments. It should be mentioned that each segment in COAT represents an optical mode for wavefront modulation and correction. Because the image or wavefront size (384×384) cannot be divided by 36, 32×32 wavefront segmentation was chosen here as the maximum, and the minimum is equal to the number of micro-lenses. In addition, the detection speed of COAT relies on the number of modulated optical modes and the modulation speed of the wavefront modulation device (spatial light modulator or deformable mirror). With the same device configuration, COAT requires much more time than the direct wavefront sensing approach, so its detection speed is not compared here. Fig. 6 shows the comparison results with a PV value of 2λ. The original distorted wavefront and the corresponding wavefront residuals after compensation are given in Fig. 6a. It can be clearly seen that the wavefront residuals of COAT become smoother as the number of segments increases. When the number of modulated optical modes in COAT increases to around 1000, the wavefront residual is almost flat but still inferior to that of TSWD. The corresponding distribution of PSFs and their central profiles are given in Figs. 6c and 6b, respectively. The light concentrates to the center, and the peak intensity is

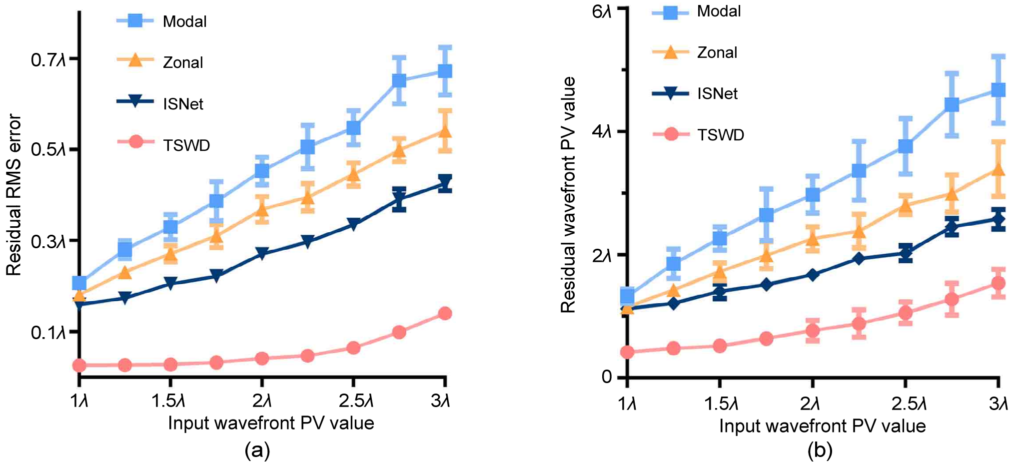

Fig. 5 Detection results with different wavefront PV values

(a) RMS wavefront error vs. input wavefront PV value; (b) Residual wavefront PV value vs. input wavefront PV value. Each group contains nine datasets. Bars indicate the standard deviations

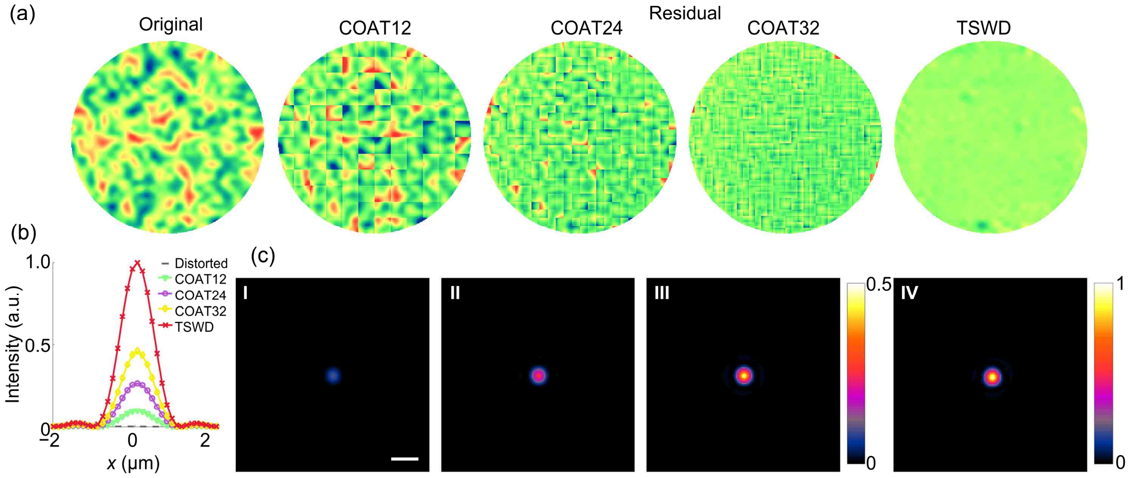

Fig. 6 Comparison results of the wavefront detection with a PV value of 2λ using COAT with 12×12, 24×24, and 32×32 segments and TSWD

(a) Original wavefront and wavefront residuals after compensation with COAT and TSWD; (b) Central intensity profiles of the compensated foci and the distorted focus; (c) Corresponding compensated focusing results with a scale bar of 3 μm improved after compensation with COAT. However, TSWD performs better, and its peak intensity is more than twice that compensated for using COAT with 32×32 segments.

The Strehl ratio (SR) is an important metric for validating wavefront compensation performance. However, because of the seriously distorted PSF, it is difficult to determine the SR for the corrected PSF. Here, we calculated the PBR of the PSFs to compare wavefront compensation performance. The PBR is defined as the ratio of the peak intensity to the average background intensity outside the focal volume (one Airy disk).

Comparison results of the PBRs are given in Fig. 7. After compensation using TSWD, the PBRs of corrected PSFs are around two orders of magnitude higher than those with conventional direct wavefront sensing approaches and also much higher than that with the indirect wavefront sensing approach, whether within or beyond the training range. A similar result is observed using ISNet. As illustrated in Fig. 7, TSWD can offer PBRs closer to the ideal situation for a complex wavefront with a PV value varying from 1λ to 2λ. Although the PBRs of corrected PSFs decay as the PV value increases, TSWD is still much better than other approaches. Its performance could be further improved by additional training with new datasets or by performing iterative detection for better compensation.

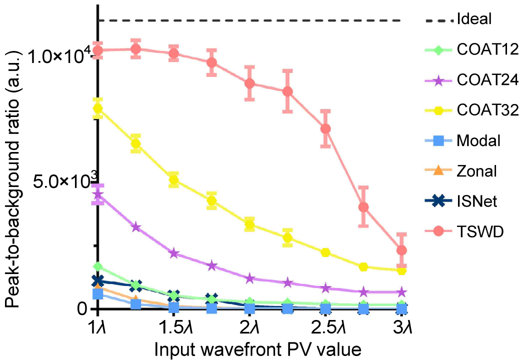

Fig. 7 Comparison of peak-to-background ratios with different methods (81 datasets)

To prove the effectiveness of our strategy, we compared the performance of TSWD with that of the modified U-net which can predict the whole wavefront directly (Vanberg et al., 2019). Fig. 8 shows the corresponding results and analysis. Comparison results on the testing datasets are shown in Fig. 8a. The intensity distribution of the PSFs becomes better after compensation with both methods, but the peak intensity compensated for using TSWD is a little higher than that of the modified U-net. Considering different kinds of wavefronts beyond the range of the training dataset, comparisons are illustrated in Figs. 8b and 8c. During the generation of wavefronts, the standard deviation of the Gaussian function controls the smoothness of wavefronts and the PV value controls the amplitude of wavefronts. Thus, we generated additional testing datasets with different parameters for further comparison. As for the flatter wavefront, which has a standard deviation of 4, TSWD shows obvious advantages. The residual of the wavefront is rougher and the peak intensity of the PSF is half that of TSWD. At the same time, TSWD maintains its advantages when the PV value becomes smaller. We have repeated experiments on a series of wavefront groups with nine different PV values and six different standard deviations of the Gaussian function. The PV value varies from 1λ to 3λ, each group containing nine datasets. The standard deviation of the Gaussian function varies from 4 to 24, each group also containing nine datasets. The comparison results of the RMS wavefront errors are given in Figs. 8d and 8e. We found that the wavefront residuals of the two methods increase as the input wavefront PV value increases, but the wavefront residuals of the modified U-net decrease first and then increase as the standard deviation increases. This means that TSWD has better generalization ability and shows advantages with various types of wavefronts, especially with a low standard deviation.

4 Discussion and conclusions

SHWS is a powerful tool for fast wavefront detection in several fields. However, SHWS is sensitive to the intensity distribution of the spot array. In adaptive optical microscopes, the commonly used wavefront reconstruction approach for SHWS, such as the modal approach, relies on centroid positioning. When detecting a wavefront with a complex distribution, centroid positioning and slope measurements would become inaccurate, and this leads to failed wavefront reconstruction. In addition, Zernike

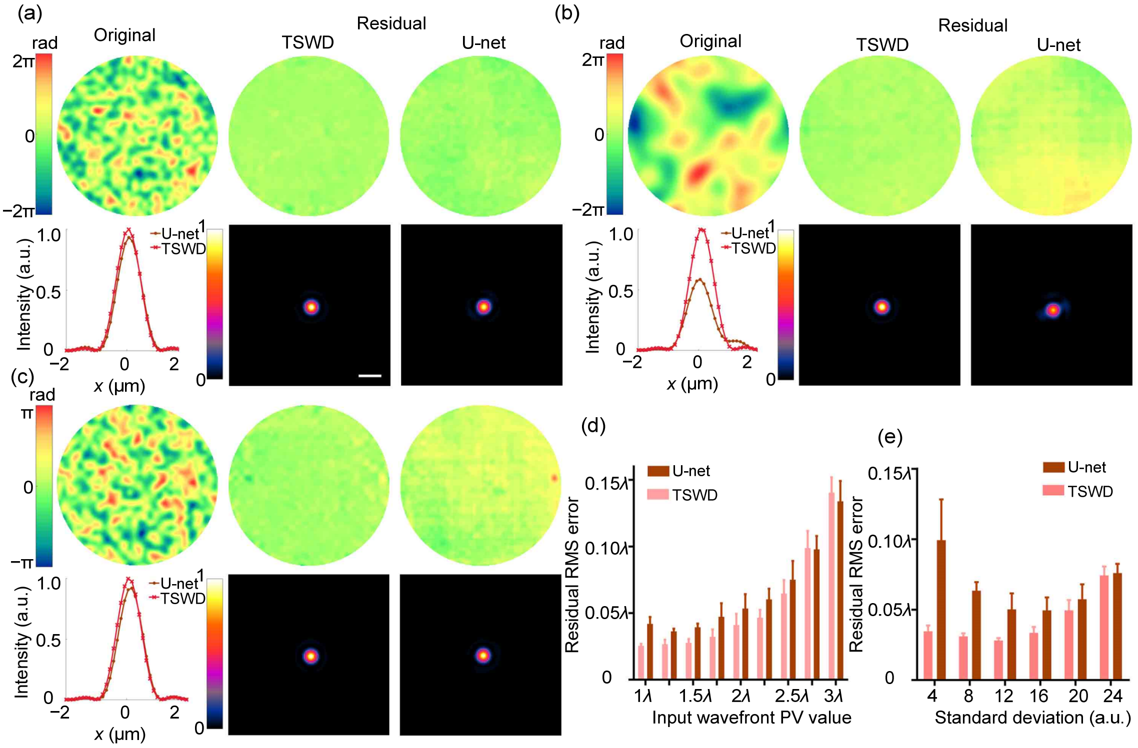

Fig. 8 Comparison of different types of wavefronts between TSWD and modified U-net

(a) Compensation results with a standard deviation of 16 and a PV value of 2λ (The original wavefront and the corresponding wavefront residual after compensation are given on the upper side; below the wavefronts are the focusing results with two methods; the central intensity profiles of the compensated foci are given on the left side with a scale bar of 3 μm); (b) Compensation results with a standard deviation of 4 and a PV value of 2λ; (c) Compensation results with a standard deviation of 16 and a PV value of 1λ; (d) RMS wavefront error vs. input wavefront PV value; (e) RMS wavefront error vs. standard deviation (Each group contains nine datasets, and bars indicate the standard deviations). References to color refer to the online version of this figure

coefficients are insufficient for characterizing a complex wavefront, and this limits the prediction accuracy of some methods that rely on Zernike coefficients. To improve the wavefront detection accuracy of SHWS, it is necessary to use the intensity distribution in each sub-region for wavefront reconstruction. If the spot intensity information is used, the detection accuracy of SHWS can be effectively improved.

In this work, we combined the PSF image based Zernike coefficient estimation for local wavefronts and the wavefront stitching method for accurate wavefront reconstruction. With the help of CNNs, the intensity distribution of every spot on SHWS can be efficiently used for local wavefront reconstruction, and Piston errors between each local wavefront can be compensated for by a neural network. Numerical simulation results show that, compared to the conventional SHWS wavefront reconstruction approaches, i.e., the recently proposed ISNet, the indirect wavefront detection method COAT, and the modified U-net, TSWD can offer higher wavefront detection accuracy and better generalization ability. The detection speed of TSWD is faster than that of the modal approach that is widely used in adaptive optical microscopes. Compared to the zonal approach and ISNet, our method can make up for the delay in the detection by its high detection accuracy. Although the networks are trained with complex wavefronts of a limited PV value range, the generalization of the models enables them effectively to detect a complex wavefront outside the training range. By additional training and optimizing the network architectures, the performance of TSWD could be further improved. For example, the effective range of accurate prediction can be enlarged by adding more kinds of wavefronts into the training dataset and the speed can be increased by compressing our model.

In conclusion, we have proposed a deep learning based method for SHWS to effectively detect a wavefront with a complex distribution. The proposed method makes up for the deficiencies of conventional methods and ISNet in complex wavefront detection. This allows SHWS to be applied to some areas which require high-precision detection of complex wavefronts. At the same time, the proposed method shortens the time of wavefront detection compared with COAT. The detection accuracy in a variety of situations and acceptable speed give our method the potential to be further applied in optical stimulation and imaging in biological science.

Contributors

Wei GONG and Ke SI designed the research. Shuwen HU, Lejia HU, Wei GONG, and Ke SI performed the research. Shuwen HU, Lejia HU, and Zhenghan LI processed the data. Shuwen HU and Lejia HU drafted the manuscript. Wei GONG and Ke SI revised and finalized the paper.

Compliance with ethics guidelines

Shuwen HU, Lejia HU, Wei GONG, Zhenghan LI, and Ke SI declare that they have no conflict of interest.

References

Booth MJ, 2014. Adaptive optical microscopy: the ongoing quest for a perfect image. *Light Sci Appl*, 3(4):e165. https://doi.org/10.1038/lsa.2014.46

Booth MJ, Neil MAA, Juškaitis R, et al., 2002. Adaptive aberration correction in a confocal microscope. *Proc Nat Acad Sci*, 99(9):5788-5792. https://doi.org/10.1073/pnas.082544799

Cheng SF, Li HH, Luo YQ, et al., 2019. Artificial intelligence-assisted light control and computational imaging through scattering media. *J Innov Opt Health Sci*, 12(4):193006. https://doi.org/10.1142/s1793545819300064

Cornea A, Conn PM, 2014. Fluorescence Microscopy: Super Resolution and Other Novel Techniques. Elsevier, London, UK, p.249.

Cui M, 2011. Parallel wavefront optimization method for focusing light through random scattering media. *Opt Lett*, 36(6):870-872. https://doi.org/10.1364/ol.36.000870

Cumming BP, Gu M, 2020. Direct determination of aberration functions in microscopy by an artificial neural network. *Opt Expr*, 28(10):14511-14521. https://doi.org/10.1364/OE.390856

Dai GM, 2008. Wavefront Optics for Vision Correction. SPIE Press, Bellingham, USA. https://doi.org/10.1117/3.769212

Drozdzal M, Vorontsov E, Chartrand G, et al., 2016. The importance of skip connections in biomedical image segmentation. Int Workshop on Deep Learning in Medical Image Analysis and Int Workshop on Large-Scale Annotation of Biomedical Data and Expert Label Synthesis, p.179-187. https://doi.org/10.1007/978-3-319-46976-8_19

Dubose TB, Gardner DF, Watnik AT, 2020. Intensity-enhanced deep network wavefront reconstruction in Shack–Hartmann sensors. *Opt Lett*, 45(7):1699-1702. https://doi.org/10.1364/OL.389895

Gómez SLS, González-Gutiérrez C, Alonso ED, et al., 2018. Improving adaptive optics reconstructions with a deep learning approach. Int Conf on Hybrid Artificial Intelligence Systems, p.74-83. https://doi.org/10.1007/978-3-319-92639-1_7

Hu LJ, Hu SW, Gong W, et al., 2019. Learning-based Shack-Hartmann wavefront sensor for high-order aberration detection. *Opt Expr*, 27(23):33504-33517. https://doi.org/10.1364/OE.27.033504

Hu LJ, Hu SW, Li YN, et al., 2020. Reliability of wavefront shaping based on coherent optical adaptive technique in deep tissue focusing. *J Biophoton*, 13(1):e201900245. https://doi.org/10.1002/jbio.201900245

Hu SW, Hu LJ, Zhang BW, et al., 2020. Simplifying the detection of optical distortions by machine learning. *J Innov Opt Health Sci*, 13(3):2040001. https://doi.org/10.1142/s1793545820400015

Ji N, 2017. Adaptive optical fluorescence microscopy. *Nat Methods*, 14(4):374-280. https://doi.org/10.1038/nmeth.4218

Jin YC, Zhang YY, Hu LJ, et al., 2018. Machine learning guided rapid focusing with sensor-less aberration corrections. *Opt Expr*, 26(23):30162-30171. https://doi.org/10.1364/OE.26.030162

Li ZH, Yu ZP, Hui H, et al., 2020. Edge enhancement through scattering media enabled by optical wavefront shaping. *Photon Res*, 8(6):954-962. https://doi.org/10.1364/PRJ.388062

Liu R, Li ZY, Marvin JS, et al., 2019. Direct wavefront sensing enables functional imaging of infragranular axons and spines. *Nat Methods*, 16(7):615-618. https://doi.org/10.1038/s41592-019-0434-7

Liu TL, Upadhyayula S, Milkie DE, et al., 2018. Observing the cell in its native state: imaging subcellular dynamics in multicellular organisms. *Science*, 360(6386):eaaq1392. https://doi.org/10.1126/science.aaq1392

Mahajan VN, Dai GM, 2007. Orthonormal polynomials in wavefront analysis: analytical solution. *J Opt Soc Am A*, 24(9):2994-3016. https://doi.org/10.1364/JOSAA.24.002994

Nishizaki Y, Valdivia M, Horisaki R, et al., 2019. Deep learning wavefront sensing. *Opt Expr*, 27(1):240-251. https://doi.org/10.1364/OE.27.000240

Paine SW, Fienup JR, 2018. Machine learning for improved image-based wavefront sensing. *Opt Lett*, 43(6):1235-1238. https://doi.org/10.1364/OL.43.001235

Park JH, Kong LJ, Zhou YF, et al., 2017. Large-field-of-view imaging by multi-pupil adaptive optics. *Nat Methods*, 14(6):581-583. https://doi.org/10.1038/nmeth.4290

Rodríguez C, Ji N, 2018. Adaptive optical microscopy for neurobiology. *Curr Opin Neurobiol*, 50:83-91. https://doi.org/10.1016/j.conb.2018.01.011

Schott S, Bertolotti J, Léger JF, et al., 2015. Characterization of the angular memory effect of scattered light in biological tissues. *Opt Expr*, 23(10):13505-13516. https://doi.org/10.1364/OE.23.013505

Swanson R, Lamb M, Correia C, et al., 2018. Wavefront reconstruction and prediction with convolutional neural networks. Adaptive Optics Systems VI, Article 10703F. https://doi.org/10.1117/12.2312590

Tang JY, Germain RN, Cui M, 2012. Superpenetration optical microscopy by iterative multiphoton adaptive compensation technique. *Proc Nat Acad Sci*, 109(22): 8434-8439. https://doi.org/10.1073/pnas.1119590109

Vanberg PO, de Xivry GO, Absil O, et al., 2019. Machine learning for image-based wavefront sensing. 33rd Conf on Neural Information Processing Systems, p.1-6.

Wang BK, Barbiero M, Zhang QM, et al., 2019. Super-resolution optical microscope: principle, instrumentation, and application. *Front Inform Technol Electron Eng*, 20(5):608-630. https://doi.org/10.1631/FITEE.1800449

Wang K, Milkie DE, Saxena A, et al., 2014. Rapid adaptive optical recovery of optimal resolution over large volumes. *Nat Methods*, 11(6):625-628. https://doi.org/10.1038/nmeth.2925

Wang K, Sun WZ, Richie CT, et al., 2015. Direct wavefront sensing for high-resolution *in vivo* imaging in scattering tissue. *Nat Commun*, 6:7276. https://doi.org/10.1038/ncomms8276

Yoon J, Lee M, Lee K, et al., 2015. Optogenetic control of cell signaling pathway through scattering skull using wavefront shaping. *Sci Rep*, 5:13289. https://doi.org/10.1038/srep13289

Yu ZP, Xia MY, Li HH, et al., 2019. Implementation of digital optical phase conjugation with embedded calibration and phase rectification. *Sci Rep*, 9(1):1537. https://doi.org/10.1038/s41598-018-38326-4

Zeng ZP, Xie H, Chen L, et al., 2017. Computational methods in super-resolution microscopy. *Front Inform Technol Electron Eng*, 18(9):1222-1235. https://doi.org/10.1631/FITEE.1601628

Shuwen HU, first author of this invited paper, received her BS degree from Tianjin University, China. She is currently a master degree candidate at the College of Optical Science and Engineering, Zhejiang University, China. Her research interests include adaptive optics, machine learning, and deep tissue imaging.

Wei GONG, corresponding author of this invited paper, is a PI at Zhejiang University School of Medicine, China. She received her BS and MS degrees from Zhejiang University, China, and her PhD degree from the National University of Singapore, Singapore. She is a special expert of the Ministry of Education (MOE) and the Outstanding Youth of Zhejiang Province. Her research interests include biomedical imaging, optical clearing, and artificial intelligence in biomedicine.

Ke SI, corresponding author of this invited paper, is a professor at the College of Optical Science and Engineering, Zhejiang University, China, and a joint professor at Zhejiang University School of Medicine. He is the Vice Director of MOE Frontier Science Center for Brain Science and Brain-Machine Integration, and the Vice Dean of the School of Brain Science and Brain Medicine. He is now a corresponding expert of *Front Inform Technol Electron Eng*. His research focuses on biophotonics, deep tissue imaging, adaptive optics, and optogenetics.